THE JOURNAL OF PHYSICAL CHEMISTRY LETTERS
A JOURNAL OF THE AMERICAN CHEMICAL SOCIETY

pubs.acs.org/JPCL Letter

$La_{0.2}Sr_{0.25}Ca_{0.45}TiO_3$ Surface Reactivity with H_2: A Combined *Operando* NEXAFS and Computational Study

F. Bassato,* S. Mauri,* L. Braglia, A. Yu. Petrov, E. Dobovičnik, F. Tavani, A. Tofoni, P. Ferrer, D. Grinter, G. Held, P. D'Angelo, and P. Torelli*

Cite This: *J. Phys. Chem. Lett.* 2024, 15, 8540−8548 Read Online

ACCESS | Metrics & More | Article Recommendations | Supporting Information

ABSTRACT: A-site doped $SrTiO_3$ is considered as a promising substitute for traditional anodic metals in solid oxide fuel cells (SOFCs). In this study, we present the reactivity of $La_{0.2}Sr_{0.25}Ca_{0.45}TiO_3$ (LCSTO), $La_{0.2}Sr_{0.7}TiO_3$ (LSTO), and $SrTiO_3$ (STO) toward H_2 by *operando* ambient pressure NEXAFS spectroscopy and theoretical spectra simulation with FDMNES code. The samples were synthesized by MBE (molecular beam epitaxy), hydrothermal, and modified-Pechini routes. We found that the reducibility of the samples depends not only on their stoichiometry but also on the morphology, which is determined by the synthetic method. The results of these experiments give insight into the reducibility of Ti^{4+} in perovskites as well as the opportunity to further optimize the synthesis of these materials to obtain the best performance for SOFC applications.

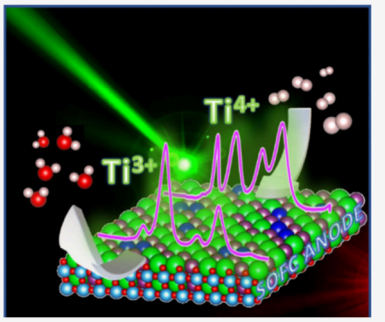

Solid oxide fuel cells (SOFCs) are the most promising type of fuel cells, offering excellent output currents and significantly reduced CO_2 emissions, a substantial environmental advantage over conventional power generation.[1−4] The state-of-the-art anodes is the cermet Ni-YSZ which has good mechanical and electrical properties but suffers from coarsening of nickel particles and coking when operated with hydrocarbons;[5−12] these drawbacks significantly hinder the device operation, and intensive research is carried out to find alternative materials that can compete with the performance of Ni-YSZ.[4,7,13] In the past few years, perovskites have drawn interest as SOFC anodes due to their high electronic conductivity in reducing atmospheres and good catalytic activity;[4,13,14] in fact, many perovskites exhibit a mixed ionic and electronic conductivity, meaning that the usual requirements of a triple phase boundary between electrode, electrolyte, and gas is not anymore necessary since the reaction can take place on the whole surface of the electrode.[15] The general formula of perovskites is ABO_3 where A and B cations are 12-fold and 6-fold coordinated to the oxygen atoms; the usual structure consists of BO_6 octahedra sharing the corners of the cube containing the A cation at the center.[13,16,17] The A-site is generally occupied by alkaline earth cations or lanthanides while transition metal ions reside on the B site, and particular attention has been given to perovskites containing Ti, Fe, and Mn due to their catalytic activity and presence of redox couples which facilitate electronic conductivity.[16,18] Notably, the perovskite structure can host different cations, and a rich defect chemistry is achieved by doping A or B sites with aliovalent cations. Nowadays, $SrTiO_3$ (STO) is being considered as a good candidate to be used as a SOFC anode due to its n-type conductivity and strong resistance to coking compared with Ni/YSZ;[19,20] although STO is quite inert toward reduction, an aliovalent doping with La^{3+} was found to increase the electronic conductivity and the reducibility of titanium,[21−23] while A-site substoichiometry enhances the ionic conductivity which mostly depends on the quantity of oxygen vacancies within the structure. The aliovalent doping with La^{3+} can be written in Kröger−Vink notation as:

$$SrTiO_3 \xrightarrow{La^{3+}} V_{Sr}^{''} + O_o^x + 2La_{Sr}^{\bullet} \quad (1)$$

Under a reducing atmosphere, oxygen vacancies are formed and Ti^{4+} is reduced to Ti^{3+}:

$$O_o^x \rightarrow \frac{1}{2}O + 2e^- + V_O^{\bullet\bullet} \quad (2)$$

$$Ti^{4+} + e^- \rightarrow Ti^{3+} \quad (3)$$

where the presence of the redox couple Ti^{4+}/ Ti^{3+} increases the electrical conductivity.[19,23] Moreover, calcium was discovered to further enhance the electronic conductivity since its introduction into $La_xSr_{0.9-x}TiO_3$ brings the d-orbitals of titanium closer.[12,24] For these reasons, $La_{0.2}Sr_{0.25}Ca_{0.45}TiO_3$ (LCSTO) appears to be an interesting candidate for anode in SOFC. The aim of this work is to study, with ambient pressure

Received: June 27, 2024
Revised: August 6, 2024
Accepted: August 8, 2024
Published: August 13, 2024

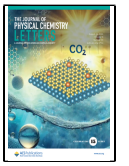

https://doi.org/10.1021/acs.jpclett.4c01900
J. Phys. Chem. Lett. 2024, 15, 8540−8548

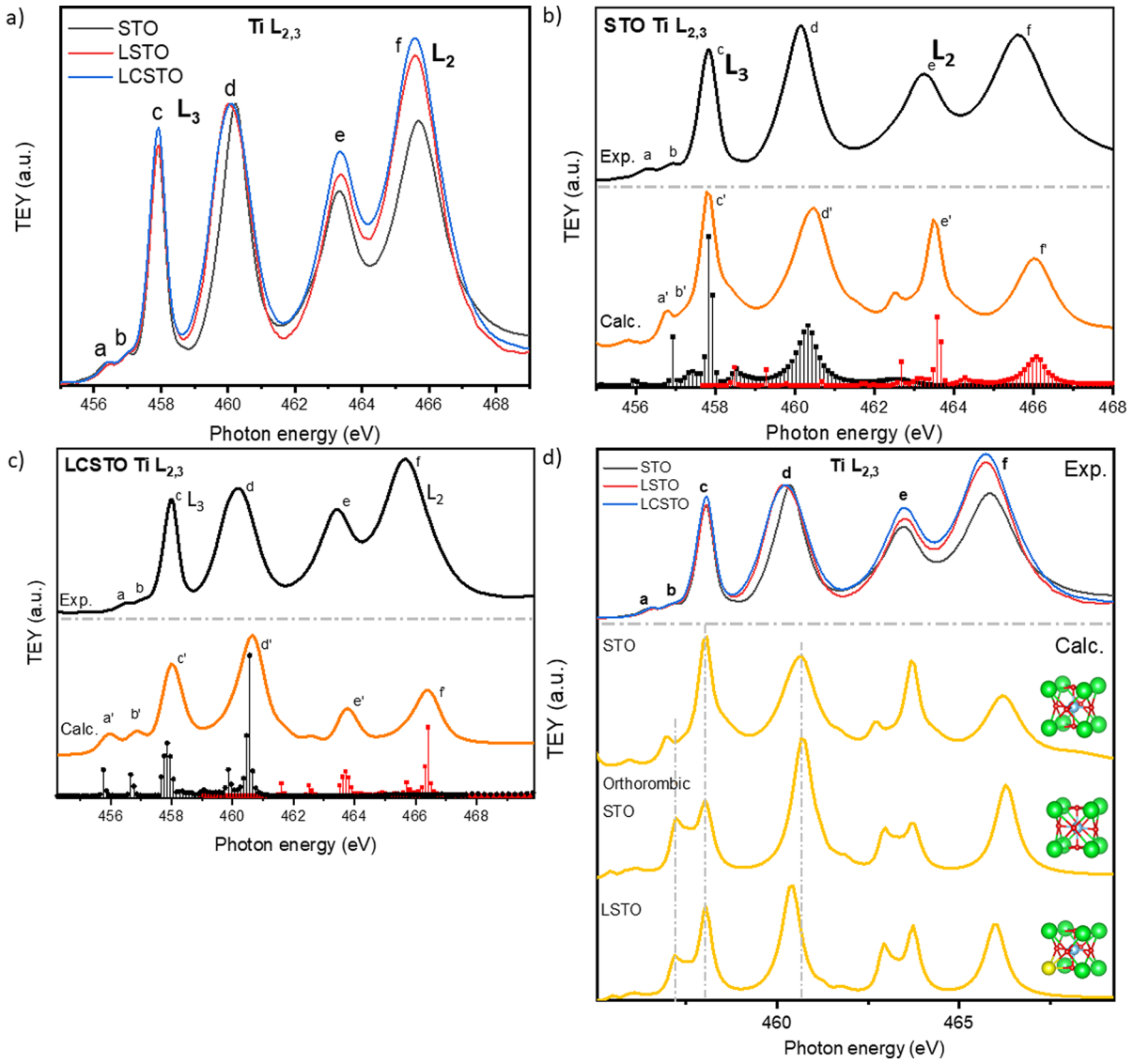

Figure 1. (a) Experimental Ti $L_{2,3}$ edges NEXAFS spectra of STO, LSTO, and LCSTO acquired at 25 °C in He (100%) atmosphere at 1 bar of pressure. (b) Experimental (top) and calculated (bottom) Ti $L_{2,3}$ edge NEXAFS spectra of STO acquired at 25 °C in He (100%) atmosphere at 1 bar of pressure. (c) Experimental (top) and calculated (bottom) Ti $L_{2,3}$ edges NEXAFS spectra of LCSTO acquired at 25 °C in He (100%) atmosphere at 1 bar of pressure. In panels b and c, the theoretical curves prior to and after convolution are shown using bars and solid lines, respectively. In the nonconvoluted theoretical spectra, the L_3 edge transitions are displayed in black while the L_2 edge features in red. (d) Top: Experimental Ti $L_{2,3}$ edge spectra of STO, LSTO and LCSTO compounds were acquired at 25 °C in He (100%) atmosphere at 1 bar of pressure. Bottom: Ti $L_{2,3}$ edges spectra calculations of cubic STO, orthorhombic STO, and La-doped cubic STO, assuming a 4+ oxidation state for Ti.

NEXAFS spectroscopy, the possible differences in reactivity between three synthetic methods of $La_{0.2}Sr_{0.25}Ca_{0.45}TiO_3$ (LCSTO): namely, MBE, hydrothermal, and modified-Pechini synthesis. NEXAFS spectroscopy is a powerful technique which can probe the L edge of 3d transition metal; if performed in total electron yield (TEY) mode, possessing a probing depth of about 4 nm,[25] it can provide surface-sensitive information on the chemical states of catalysts and reactants.[26−28] In particular, we focused on the reducibility of titanium by performing all the NEXAFS experiments in 1 bar of H_2 at 350 °C and, to obtain a deeper understanding of all the possible scenarios, the NEXAFS spectra were supported by theoretical calculations. In particular, the FDMNES code has been employed to simulate the spectral features and to gain important insight into the spectroscopic fingerprints of Ti sites in perovskites. Besides ambient pressure NEXAFS, the samples were characterized also by XRD, SEM, and XPS to gain a complete overview of their chemical and morphological features.

A series of samples comprising STO, LSTO, and LCSTO have been prepared with different methods: MBE, hydrothermal, and Pechini. The MBE samples were grown in a dedicated system on commercially available STO (001) substrates and are in single-crystal form. The hydrothermal and Pechini samples are in powder form, and the details of the synthesis are presented in Experimental Methods. The hydrothermal and Pechini samples were first characterized with XRD to assess their purity (while the obvious crystallinity of MBE grown samples has been controlled with RHEED pattern during growth): the XRD patterns of LCSTO powders show all the reflections of the orthorhombic perovskite structure, although the sample LCSTO Pechini contains

https://doi.org/10.1021/acs.jpclett.4c01900
J. Phys. Chem. Lett. 2024, 15, 8540−8548

some residual TiO_2 (~2% wt) (Figures S1 and S2). Figure S2 is a closer inspection of the (200) reflection: the diffractograms of LSTO are shifted toward higher angles with respect to the undoped STO due to the substitution of Sr^{2+} (ionic radius = 132 pm) ions with the smaller La^{3+} (69 pm), giving rise to a lattice shrinking. This result hints at a successful incorporation of the dopants in the perovskite crystal structure. Moreover, a further shift between LSTO and LCSTO is also visible: according to Aljaberi and Irvine, the codoping with Ca^{2+} ions (114 pm) induces a unit cell deformation from cubic to orthorhombic, depending on the amount of calcium present in the sample.[29] An SEM analysis was performed to obtain information on the particles' morphology. As reported in Figure S3 the two synthetic methods gave quite different outcomes: hydrothermal LCSTO is composed of micrometrics aggregates with irregular polyhedric shapes, while LCSTO Pechini is, on the contrary, composed of smaller pebble-like particles. The reduced particle size of LCSTO Pechini (Figure S4) could be ascribed to the different synthetic procedure which involved a lower-temperature treatment (1000 °C vs 1200/1300 °C) along with the use of a different Ti precursor.

The surface chemistry of these samples was investigated via XPS analysis: the survey spectra shown in Figure S5 present all the expected peaks for the LCSTO stoichiometry; in addition, a small Na 1s peak is visible in hydrothermal LCSTO ascribed to NaOH used in the synthesis. As reported in the literature,[30,31] the Sr 3d core level can be fitted with one doublet for bulk and the other for surface Sr−O bonds (Figure S6c,d). Ti 2p core level was fitted with two doublets in good agreement with the literature:[32−35] the most intense is ascribed to a Ti^{4+} state, while the lesser is related to Ti^{3+} (~9% at.) present in LCSTO because of a trivalent doping. The O 1s peak can be fitted with 3 main components[30,36−39] which are reported in Tables S2 and S3: O_1 can be ascribed to lattice oxygen, while O_2 and O_3 are consistent with the presence of $V_O^{\bullet\bullet}$ in the neighboring sites and surface −OH, respectively. A minor contribution (O_s) was also included in the fit, accounting for the sample holder. The typical La 3d doublet has a characteristic shakeup feature while there is no presence of La_2O_3, whose $3d_{5/2}$ peak falls at 834.5 eV,[36] therefore hinting at a complete insertion of La in the perovskite lattice (Figure S6e,f). The stoichiometries obtained from XPS analysis are displayed in Table S4 and are in good agreement with the theoretical values, with Sr being a little over stoichiometric; this discrepancy is related to alkaline-earth cation surface migration, a phenomenon that is known to happen in perovskites.[31,40] Overall, the XRD and XPS analyses confirmed the successful synthesis of LCSTO, with both methods, leading to powders which possess the right perovskite structure with the expected stoichiometry and absence of secondary phases.

In this section the NEXFAS spectra of the Ti $L_{2,3}$ edge in the different samples are presented together with the spectra simulation and interpretation. The experimental Ti $L_{2,3}$ edge spectrum of STO shows the typical structures related to Ti^{4+} sites with octahedral coordination,[41] labeled as **a**−**f** in Figure 1a. These structures originate when the d^0 ground state of Ti^{4+} is excited to the $2p^53d^1$ configuration in which a hole is present in one of the six 2p states while an electron occupies one of the ten 3d states. Spin orbit coupling gives rise to two absorption edges (L_2 and L_3) with a spin orbit splitting of 5.42 eV, in agreement with the literature.[42,43] A detailed description of the spectral features is given in the Supporting Information.

The experimental spectra of LSTO and LCSTO show the same spectral features of STO, although small differences are appreciable: the pre-edge structures **a** and **b** are less resolved as a consequence of the broadening of structure **b**; moreover, structure **d** appears broader and shifted to lower photon energies with respect to the STO spectrum. To obtain a deeper interpretation of the Ti $L_{2,3}$-edge spectra and to address the spectral modifications which can be observed during the interaction of the perovskite surfaces with H_2, theoretical simulations of the spectra have been carried out by means of the FDMNES code.[44,45] Figure 1b,c compares the experimental and calculated spectra of STO and LCSTO. For the calculation, the structural model employed is described in detail in Figure S9 of the Supporting Information. The theoretical simulation of the Ti $L_{2,3}$ edge spectrum of STO is in good agreement with the experimental one: the convolution of the calculated transitions (reported as black and red bars for the L_3 and L_2 edge contributions, respectively) gives rise to features **a′**−**f′**, whose intensities and energy positions correctly reproduce those of the experimental data. The different peak width observed between the **c** and **d** structures in the L_3 edge is well reproduced by the simulations (structure **d′** is broader than **c′**), confirming a larger energetic distribution of the transitions toward e_g-type orbitals (peak **d′**) with respect to the t_{2g} ones (peak **c′**), as previously reported.[42] Having benchmarked and established the reliability of our theoretical framework, we maintained the same FDMNES theoretical parameters and employed a different structural model (see model 3 of Figure S9) to simulate the Ti $L_{2,3}$ edge spectra of LCSTO, whose experimental and simulated spectra are presented in Figure 1c. The calculated spectrum of Figure 1c has been obtained from the average of separate calculations where all the possible LCSTO unit cell configurations have been considered, since La, Ca, and Sr atoms can be arranged in 17 different ways in the first coordination shell of a Ti atom (see Figure S10 for further details). The calculated spectrum correctly reproduces all of the experimental features of LCSTO. A broadening of the t_{2g}-related structures (**b′**, **c′**, and **e′**) is observed with respect to the undoped STO, in agreement with what is observed experimentally: the calculations show that this is due to a larger energetic distribution of the related transitions. Moreover, when comparing the pre-edge transitions of the calculated spectra of STO and LCSTO (Figure S11 of the Supporting Information), one can observe that structure **b′** falls at a slightly different photon energy (ΔE = 0.2 eV), thus giving a possible explanation for the broadening of structure **b′** observed experimentally for LCSTO. To further investigate the spectral differences observed between STO and LCSTO, complementary simulations have been carried out as shown in Figure 1d: we simulated the Ti L edge spectrum of STO with an orthorhombic unit cell (Model 2 in Figure S9 of the Supporting Information) in order to investigate the spectral modifications caused by the crystal structure distortion. Comparing the simulated spectra of cubic and orthorhombic STO, an energy shift of the pre-edge structure **b** can be observed; moreover, its intensity is enhanced in the orthorhombic STO, showing how the pre-edge structures of STO are directly related to the crystal field of the Ti atoms, confirming what was previously reported with the use of semiempirical methods.[42] We also investigated the role of La substitution in a cubic STO lattice (Figure 1d), exploiting model 4 of Figure S9 as the input structure for the calculations.

https://doi.org/10.1021/acs.jpclett.4c01900
J. Phys. Chem. Lett. 2024, 15, 8540−8548

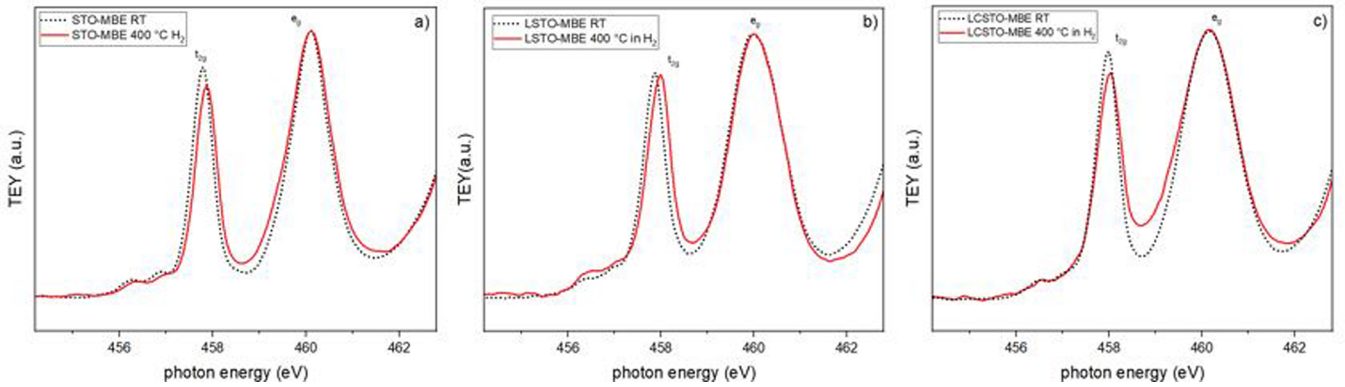

Figure 2. NEXAFS spectra of MBE thin films: STO, LSTO, and LCSTO. Only the Ti L_3 edge is shown for clarity.

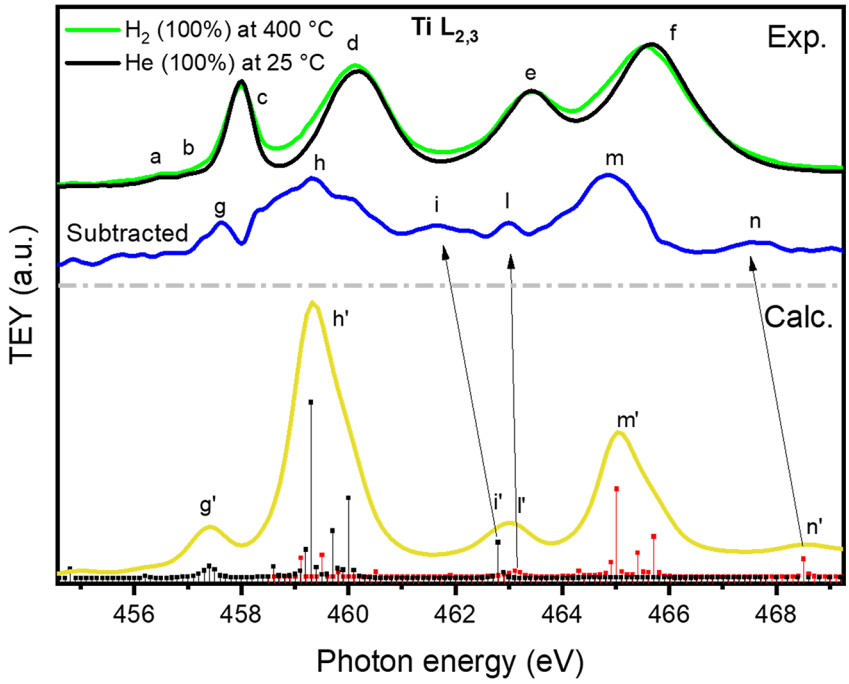

Figure 3. Top: Experimental Ti $L_{2,3}$ edges spectra of $La_{0.2}Ca_{0.45}Sr_{0.25}TiO_3$ acquired at 25 °C in He (100%) atmosphere (black) and at 400 °C in H_2 (100%) atmosphere (green). Blue spectrum was obtained by subtracting the black spectrum to the green one. Bottom: Ti $L_{2,3}$ edges spectra simulation of $La_{0.2}Ca_{0.45}Sr_{0.25}TiO_3$, assuming a 3+ oxidation state for Ti. The theoretical curve prior to and after convolution is shown by using bars and solid lines, respectively. In the nonconvoluted theoretical spectrum, the L_3 edge transitions are displayed in black while the L_2 edge features in red.

In this case, the substitution of a Sr atom by a La in the STO unit can generate eight geometrically equivalent configurations; thus, we only calculated the spectrum of the one shown in Figure S9. In the calculated LSTO spectrum, we observe a redistribution of t_{2g} type transitions (pre-edge structures and peak **c**) similar to that of the orthorhombic STO but less enhanced. More interestingly, peak **d** is shifted toward lower photon energies, consistent with the experimental observations. This suggests a decrease of the octahedral crystal field splitting ΔO_h as a direct consequence of La doping; performing two separated calculations for the orthorhombic $SrTiO_3$ and cubic $La_xSr_{1-x}TiO_3$ allowed discrimination of the effects induced by the structural distortions and chemical doping.

To investigate the effect of A-site doping in $SrTiO_3$ we decided to study first, as a model system, the MBE samples with *operando* NEXAFS at the Ti $L_{2,3}$ edge. In Figure 2a, when STO is exposed to H_2 at 400 °C, we can clearly see that the two spectra are very similar, hinting at a high stability of STO in a reducing atmosphere. Notably, also LSTO does not display significant changes, meaning that La doping also does not change remarkably the STO reactivity. Conversely, the codoping with Ca in LCSTO leads to a notable rise of the t_{2g}–e_g valley as shown in Figure 2c.

To correlate the spectroscopic modifications observed during exposure to H_2 with the reducibility of the samples, we performed theoretical DFT simulations. Experimentally, the most evident modifications observed in LCSTO before and after the heating ramp in H_2 are related to the rise of the valley between **c** and **d** structures and to the broadening of the pre-edge region (structures **a** and **b**), clearly visible in the upper panel of Figure 3. From the subtraction of the two spectra, the blue spectrum of Figure 3 has been obtained which consists of six main features labeled as **g**–**n**. In this particular case, for the

https://doi.org/10.1021/acs.jpclett.4c01900
J. Phys. Chem. Lett. 2024, 15, 8540−8548

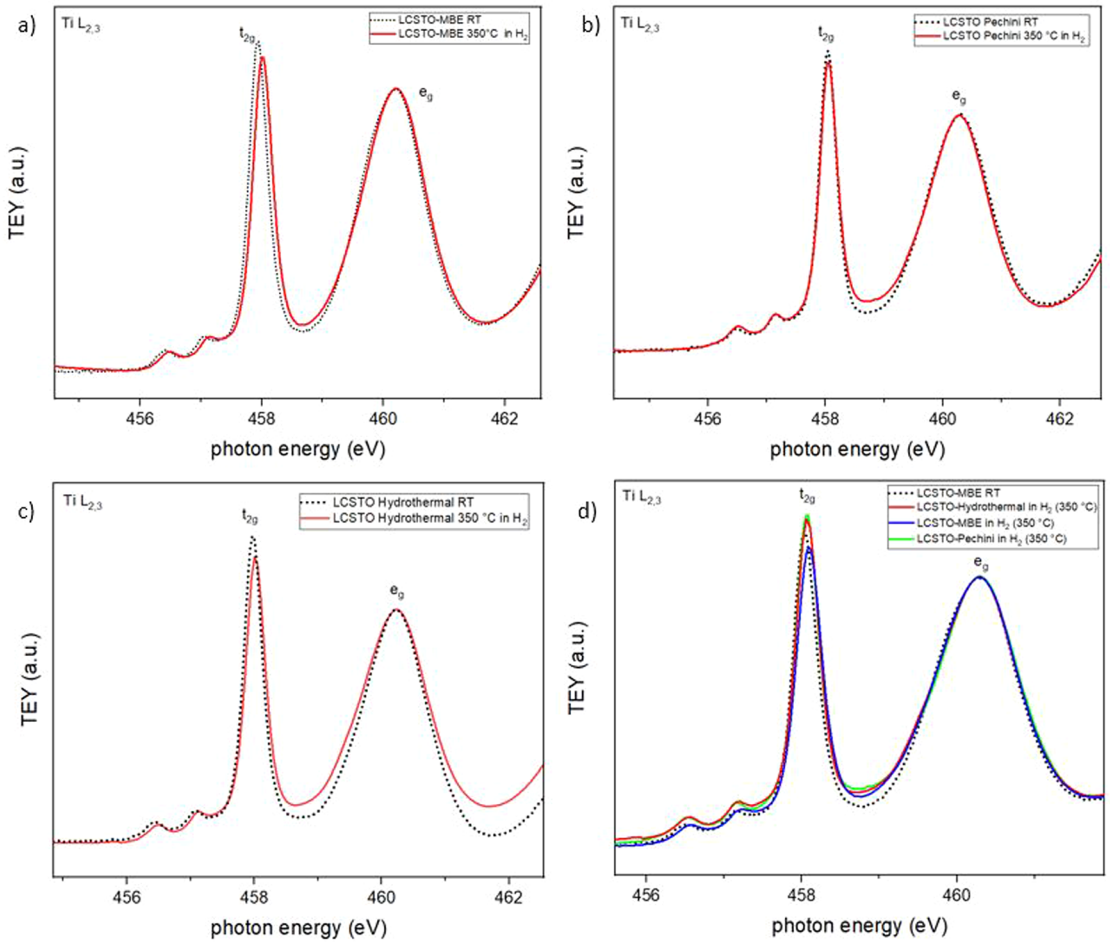

Figure 4. Ti L_3 edge of LCSTO samples: RT vs 350 °C in H_2 (100%).

spectra subtraction performed in Figure 3, the two Ti L edge spectra have been normalized at the t_{2g} peak (labeled as **c** in the figure) in order to extract the line shape of the X-ray absorption spectrum of the Ti^{3+} species. We hypothesize that heating under a reducing atmosphere could promote the activation of H_2 on the surface oxygen sites and the consequent H_2 dissociation to yield water desorption. This process would result in the formation of an oxygen vacancy and a Ti^{3+} site as charge compensation. In order to verify this hypothesis, we calculated the Ti $L_{2,3}$ edges NEXAFS spectrum of a Ti^{3+} photoabsorber in LCSTO (model 5 of Figure S9), having an oxygen vacancy in the first coordination shell (see Supporting Information for details). The resulting spectrum is shown in the bottom panel of Figure 3: we observe an excellent agreement between the experimental subtracted spectrum and the calculated one. The energy position and the relative intensity of the main structures (**g**, **h**, **l**, **m**) is perfectly reproduced in the calculation; **i′** (L_3 edge) and **n′** (L_2 edge) features of the calculated spectrum are present at slightly lower energies in the experimental one. For this reason, **i** and **l** features appear as a doublet, while in the calculated spectrum **i′** and **l′** are almost superimposed, appearing as a single structure in the convoluted spectrum.

Through the calculated spectrum of Figure 3 we therefore were able to validate the hypothesis of the formation of Ti^{3+}-$V_O^{\bullet\bullet}$ sites consequent to the interaction of the perovskite surface with H_2; moreover, we proved that the subtracted spectrum of Figure 3 is related to Ti^{3+} photoabsorbers with a distorted octahedral coordination (see model 5, Figure S9 in the Supporting Information). With the help of DFT simulations, which allowed us to label the fingerprint of Ti^{3+} in NEXAFS spectra, we also confirmed that LCSTO is an interesting candidate, more than STO and LSTO, for SOFC anodes.

Having obtained these results on the MBE model systems, we wanted to investigate how different chemical syntheses could affect the redox properties of LCSTO, specifically two samples obtained by hydrothermal and modified-Pechini routes. The Ti L_3 edge for Pechini and hydrothermal LCSTO are shown together with the Ti edge of the MBE grown sample in Figure S12 of the Supporting Information; the perfect correspondence of the spectra proves once more the quality of the synthesized powders, given the fact the NEXAFS spectra are extremely sensitive to the details of the electronic structure even more than the XPS, thus demonstrating the perfect coincidence of the electronic structure of the different samples. In Figure 4, the Ti L_3 edge is shown recorded at room temperature, in He atmosphere (1 bar of pressure), and in pure H_2 at 1 bar of pressure and about 350 °C. As reported in Figure 4a, LCSTO-MBE displays little change, while the powder samples exhibit a higher quantity of Ti^{3+}. In detail, the MBE sample shows the smaller activity and the Pechini the higher activity, while hydrothermal is somewhere in between the two. Given the strong similarities

https://doi.org/10.1021/acs.jpclett.4c01900
J. Phys. Chem. Lett. 2024, 15, 8540−8548

between the different samples from the point of view of the crystal and electronic structure, we consider that the morphology of the surface is at the base of the different reactivity of the samples. This is rationalized as follows: the Pechini sample presents smaller particles (about 200 nm) while the hydrothermal leads to micrometric agglomerates and the MBE presents obviously an atomic flat surface; thus, the Pechini has the highest density of defects at surface (step edges, corners, etc.) followed by the hydrothermal and the MBE, and these sites are those responsible for the activity toward hydrogen.

In this study, the surface reactivity of A-site doped $SrTiO_3$ has been thoroughly studied by *operando* NEXAFS interpreted with the help of theoretical simulations. The Ti $L_{2,3}$ edge was collected at around 400 °C in H_2 flow to follow the reduction process of the perovskite. The experiment conducted on a model surface prepared by MBE proved the successful doping strategy for the sample $La_{0.2}Sr_{0.25}Ca_{0.45}TiO_3$ in increasing the material reactivity, an essential property to guarantee adequate electrical conductivity. Moreover, we compared how different chemical synthesis methods result in different outcomes in terms of surface reactivity: LCSTO Pechini is slightly more reactive than the hydrothermal one, probably owing to its smaller particle size and possible presence of surface defects. We think that this work could give fundamental insights into the surface properties of A-site doped $SrTiO_3$, which can lead to an optimization of the synthesis process. We also proved the successful multitechnique approach to characterize the properties of perovskites and to evaluate their possible applications.

EXPERIMENTAL METHODS

Synthesis of the Samples. The following chemicals were used as received without further purification: Strontium hydroxide octahydrate (Alfa Aesar), titanium(IV) isopropoxide (>97%, Alfa Aesar), titanium(IV) oxide (>99.98%, rutile, Sigma-Aldrich), lanthanum(III) nitrate hexahydrate (99.9%, Alfa Aesar), calcium chloride dihydrate (Sigma-Aldrich), citric acid monohydrate (ACS 99−102%, Alfa Aesar), and ammonia (30% w/w solution, Sigma-Aldrich). $La_{0.2}Sr_{0.25}Ca_{0.45}TiO_3$ (LCSTO) was prepared by both hydrothermal and modified Pechini routes. For the hydrothermal synthesis 0.239 g (3 mmol) of TiO_2, 0.199 g (0.75 mmol) of $Sr(OH)_2$, 0.259 g (0.6 mmol) of $La(NO)_3$, and 0.198 g (1.35 mmol) of $Ca(Cl)_2$ were added to 50 mL of a 3 M NaOH solution. After being stirred for 20 min, the mixture was transferred in a Teflon liner, sealed in an autoclave, and heated at 220 °C for 20 h. The product was washed twice with distilled water and dried at 80 °C overnight. Subsequently, the powder was calcined in air first at 1200 °C for 12 h and then additionally at 1300 °C for 10 h. The modified Pechini synthesis was performed by adapting a known procedure:[46] stoichiometric amounts of $Ti(iOPr)_4$, $Sr(OH)_2$, $La(NO_3)_3$, and $CaCl_2$ were mixed in 50 mL of distilled water. Then, citric acid monohydrate was added in a molar ratio (1.9:1= acid: sum of cations), and the pH of the solution was adjusted to 6,5 with ammonium hydroxide. The reaction mixture was stirred for 12 h at 80 °C and then fired at 380 °C for 2 h to remove the organic content. The resulting powder was ground in an agate mortar and calcined for 12 h at 1000 °C. LCSTO-MBE was deposited in an oxygen assisted MBE chamber present at APE-HE growth and characterization cluster.[47] The film was grown by a shuttered method repeating the layered structure of perovskite in the direction $(001)_c$ when the $La_{0.2}Sr_{0.25}Ca_{0.45}$ atomic layer is followed by the TiO_2 atomic layer: this method allows obtaining and following a precise stoichiometric calibration. After the right stoichiometry 1:1 was found on a calibration substrate, 10%-off stoichiometry is calculated and grown on a new substrate. The sample was grown in an oxygen atmosphere ($P = 5 \times 10^{-6}$ mbar, $T = 730$ °C) on a STO (001) substrate: the growth speed was about 4 Å/min. $La_{0.2}Sr_{0.7}TiO_3$ (LSTO) and $SrTiO_3$ (STO) films were prepared under the same conditions described above and used as reference compounds.

Powder X-ray Diffraction. Diffraction patterns were collected with Philips X'Pert and Panalytical Empyrean diffractometers in Bragg−Brentano mode. The X-ray source was a Cu anode operating at 40 kV and 30 mA. The diffraction patterns were acquired in the 20−80° 2θ range with $\Delta(2\theta) = 0.02°$ and an exposure time of 3 s/step. The identification of the crystalline phases was done by consulting bibliographical references.

XPS Measurements. The XPS measurements were performed with the instrument present at APE-HE beamline at Elettra Sincrotrone, Italy.[47] The source energy was Al Kα and the instrument was calibrated with a Au reference ($4f_{7/2}$ peak set equal to 84 eV). The pass energy was set to 100 eV for the surveys and to 50 eV for a single element scan, while the dwell time was set to 1500 ms for all the scans. Charging effects were corrected by imposing the Ag $3d_{5/2}$ peak to 368.3 eV. The core levels were all fitted with a Voigt function after a Shirley background subtraction. The surface quantitative analysis was performed by comparing the peak areas after normalizing on the nominal cross section for each orbital: the A-site stoichiometry was calculated by imposing the normalized area of Ti to unity and calculating the ratio (Sr + La+ Ca)/Ti.

SEM Microscopy. Scanning electron microscopy (SEM) was performed with a field-emission SEM Zeiss SUPRA 40 operating at 5 keV, with a W.D. of 6 mm and a nominal point resolution of 1.5 nm. The employed source was a Schottky field gun, and the signal was collected with an Everhart-Thornley detector.

Operando NEXAFS Experiment. *Operando* NEXAFS experiments were performed both at APE beamline (Elettra Sincrotrone, Italy) and VerSOx B07 beamline (Diamond Light Source, UK) by exploiting the reaction cells described elsewhere.[48−50] For the measurements, the samples were drop cast on the sample holder or, in the case of thin films, directly glued with conductive silver paint. The exslits of the beamlines were set at 50 μm and the achieved resolution was ∼50 meV. The measurements were performed in TEY by following the procedure shown in Figure S7, and the total gas flux was set to 50 sccm for all the measurements. NEXAFS spectra were normalized by imposing the L_3 pre-edge and L_2 tail to the same intensity. The background was subtracted with a 6-points spline, and in the case of Ti $L_{2,3}$ edge, the spectra were normalized also on the e_g peak to underline the possible presence of Ti^{3+}.

Theoretical Simulations: FDMNES Code. The Ti $L_{2,3}$-edge NEXAFS spectra of $SrTiO_3$, $LaTiO_3$, and $La_{0.2}Sr_{0.25}Ca_{0.45}TiO_3$ have been simulated using the Finite Difference Method Near Edge Structure code (FDMNES).[44,45] FDMNES employs density functional theory (DFT) with an optionally spin-dependent local exchange−correlation potential. For all calculations, the muffin-tin (MT) approximation was used to model the potential, ensuring a 19% overlap of the MT spheres. Quadrupolar transitions and relativistic effects have been included in the calculations, which were also corrected by a subsequent time-dependent DFT (TDDFT) calculation

https://doi.org/10.1021/acs.jpclett.4c01900
J. Phys. Chem. Lett. 2024, 15, 8540−8548

making use of an internal local kernel implemented in FDMNES. The theoretical spectra were calculated using clusters built from the crystallographic structures of the three materials employing cutoff radii of 6 Å from the chosen photoabsorber atom: this value has been chosen as it leads to a theoretical spectrum where the main features of $L_{2,3}$ edges are well reproduced and convergence is achieved when further increasing the cutoff radius. An example of the input employed for the calculations is described in the Supporting Information.

■ ASSOCIATED CONTENT

Supporting Information

The Supporting Information is available free of charge at https://pubs.acs.org/doi/10.1021/acs.jpclett.4c01900.

XRD patterns, SEM images and particle size analysis, XPS core levels, experimental details on *operando* experiments, details on theoretical modeling, input structure, comparison between pre-edge structures of calculated STO and LCSTO NEXAFS spectra, and cif data (PDF)

Transparent Peer Review report available (PDF)

■ AUTHOR INFORMATION

Corresponding Authors

F. Bassato − *Istituto Officina dei Materiali IOM−CNR, Laboratorio TASC, Trieste I-34149, Italy; Department of Physics, University of Trieste, Trieste 34127, Italy;* orcid.org/0000-0002-2775-2662; Email: bassato@iom.cnr.it

S. Mauri − *Istituto Officina dei Materiali IOM−CNR, Laboratorio TASC, Trieste I-34149, Italy;* orcid.org/0000-0003-2183-4293; Email: mauri@iom.cnr.it

P. Torelli − *Istituto Officina dei Materiali IOM−CNR, Laboratorio TASC, Trieste I-34149, Italy*; Email: torelli@iom.cnr.it

Authors

L. Braglia − *Istituto Officina dei Materiali IOM−CNR, Laboratorio TASC, Trieste I-34149, Italy;* Present Address: Area Science Park, Padriciano 99, Trieste, Italy; orcid.org/0000-0003-0796-3670

A. Yu. Petrov − *Istituto Officina dei Materiali IOM−CNR, Laboratorio TASC, Trieste I-34149, Italy*

E. Dobovičnik − *Department of Engineering and Architecture, University of Trieste, Trieste 34127, Italy*

F. Tavani − *Department of Chemistry, University of Rome "La Sapienza", 00185 Rome, Italy;* orcid.org/0000-0003-3279-1081

A. Tofoni − *Department of Chemistry, University of Rome "La Sapienza", 00185 Rome, Italy;* orcid.org/0000-0003-1935-4063

P. Ferrer − *Diamond Light Source, Oxfordshire OX11 0DE, U.K.;* orcid.org/0000-0001-9807-7679

D. Grinter − *Diamond Light Source, Oxfordshire OX11 0DE, U.K.;* orcid.org/0000-0001-6089-119X

G. Held − *Diamond Light Source, Oxfordshire OX11 0DE, U.K.;* orcid.org/0000-0003-0726-4183

P. D'Angelo − *Department of Chemistry, University of Rome "La Sapienza", 00185 Rome, Italy;* orcid.org/0000-0001-5015-8410

Complete contact information is available at: https://pubs.acs.org/10.1021/acs.jpclett.4c01900

Notes

The authors declare no competing financial interest.

■ ACKNOWLEDGMENTS

This work has been performed in the framework of the Nanoscience Foundry and Fine Analysis (NFFA-MUR Italy Progetti Internazionali) facility. Diamond Light Source is thanked for the provision of beamtime (exp. SI33111-1). We acknowledge financial support under the National Recovery and Resilience Plan (PNRR), Mission 4, Component 2, Investment 1.1, Call for tender No. 1409 published on 14.9.2022 by the Italian Ministry of University and Research (MUR), funded by the European Union − Next Generation EU− Project Title A-LENS Atomic-level understanding of solid-oxide fuel cell processes− CUP D53D23019420001-Grant Assignment Decree No. 1381 adopted on 01/09/2023 by the Italian Ministry of Ministry of University and Research (MUR). L.B. acknowledges the "Programma Nazionale della Ricerca (PNR)" grant J95F21002830001 with title "FAIR-by-design".

■ REFERENCES

(1) Felli, A.; Mauri, S.; Marelli, M.; Torelli, P.; Trovarelli, A.; Boaro, M. Insights into the Redox Behavior of Pr0.5Ba0.5MnO3-δ-Derived Perovskites for CO2 Valorization Technologies. *ACS Appl. Energy Mater.* **2022**, *5* (6), 6687−6699.

(2) Ormerod, R. M. Solid Oxide Fuel Cells. *Chemical Society Reviews.* **2003**, *32*, 17−28.

(3) Yang, G.; Su, C.; Chen, Y.; Tadé, M. O.; Shao, Z. Nano La0.6Ca0.4Fe0.8Ni0.2O3-δ Decorated Porous Doped Ceria as a Novel Cobalt-Free Electrode for "Symmetrical" Solid Oxide Fuel Cells. *J. Mater. Chem. A Mater.* **2014**, *2* (45), 19526−19535.

(4) Zhou, J.; Shin, T. H.; Ni, C.; Chen, G.; Wu, K.; Cheng, Y.; Irvine, J. T. S. In Situ Growth of Nanoparticles in Layered Perovskite $La_{0.8}Sr_{1.2}Fe_{0.9}Co_{0.1}O_{4-\delta}$ as an Active and Stable Electrode for Symmetrical Solid Oxide Fuel Cells. *Chem. Mater.* **2016**, *28* (9), 2981−2993.

(5) Zhu, T.; Fowler, D. E.; Poeppelmeier, K. R.; Han, M.; Barnett, S. A. Hydrogen Oxidation Mechanisms on Perovskite Solid Oxide Fuel Cell Anodes. *J. Electrochem. Soc.* **2016**, *163* (8), F952−F961.

(6) Qiu, P.; Yang, X.; Wang, W.; Wei, T.; Lu, Y.; Lin, J.; Yuan, Z.; Jia, L.; Li, J.; Chen, F. Redox-Reversible Electrode Material for Direct Hydrocarbon Solid Oxide Fuel Cells. *ACS Appl. Mater. Interfaces* **2020**, *12* (12), 13988−13995.

(7) Paloukis, F.; Papazisi, K. M.; Dintzer, T.; Papaefthimiou, V.; Saveleva, V. A.; Balomenou, S. P.; Tsiplakides, D.; Bournel, F.; Gallet, J. J.; Zafeiratos, S. Insights into the Surface Reactivity of Cermet and Perovskite Electrodes in Oxidizing, Reducing, and Humid Environments. *ACS Appl. Mater. Interfaces* **2017**, *9* (30), 25265−25277.

(8) Cavazzani, J.; Bedon, A.; Carollo, G.; Rieu, M.; Viricelle, J. P.; Glisenti, A. Rational Development of IT-SOFC Electrodes Based on the Nanofunctionalization of La0.6Sr0.4Ga0.3Fe0.7O3 with Oxides. Part 2: Anodes by Means of Manganite Oxide. *ACS Appl. Energy Mater.* **2023**, *6* (1), 141−150.

(9) Hou, B.; Lin, M.; Wei, Y.; Lu, X.; Mi, S.; Bao, C. First-Principles Study on Exsolution of Ni and Ni−M (M = Fe, Co, Cr, Cu) Alloy Nanoparticles in the SrTiO 3 Model as the Perovskite Cathode of Solid Oxide Electrolysis Cells. *J. Phys. Chem. C* **2024**, *128*, 2867−2875.

(10) Shaikh, S. P. S.; Muchtar, A.; Somalu, M. R. A Review on the Selection of Anode Materials for Solid-Oxide Fuel Cells. *Renewable and Sustainable Energy Reviews. Elsevier Ltd June* **2015**, *51*, 1−8.

(11) Li, X.; Liu, M.; Lai, S. Y.; Ding, D.; Gong, M.; Lee, J. P.; Blinn, K. S.; Bu, Y.; Wang, Z.; Bottomley, L. A.; Alamgir, F. M.; Liu, M. In Situ Probing of the Mechanisms of Coking Resistance on Catalyst-Modified Anodes for Solid Oxide Fuel Cells. *Chem. Mater.* **2015**, *27* (3), 822−828.

(12) Aljaberi, A. D.; Irvine, J. T. S. Crystal Structure of A-Site Deficient La0.2Sr0.7-XCaxTiO3 Perovskite at Ambient Conditions and High Temperatures: A Neutron Powder Diffraction Study. *Dalton Transactions* **2015**, *44* (23), 10828−10833.
(13) Yaqub, A.; Savaniu, C.; Janjua, N. K.; Irvine, J. T. S. Preparation via a Solution Method of La0.2Sr 0.25Ca0.45TiO3 and Its Characterization for Anode Supported Solid Oxide Fuel Cells. *J. Mater. Chem. A Mater.* **2013**, *1* (45), 14189−14197.
(14) Yaqub, A.; Janjua, N. K.; Savaniu, C.; Irvine, J. T. S. Synthesis and Characterization of B-Site Doped La0.20Sr0.25Ca0.45TiO3 as SOFC Anode Materials. *Int. J. Hydrogen Energy* **2015**, *40* (1), 760−766.
(15) Hui, S.; Petric, A. Evaluation of Yttrium-Doped SrTiO 3 as an Anode for Solid Oxide Fuel Cells. *J. Eur. Ceram Soc.* **2002**, *22*, 1673−1681.
(16) Neagu, D.; Irvine, J. T. S. Enhancing Electronic Conductivity in Strontium Titanates through Correlated A and B-Site Doping. *Chem. Mater.* **2011**, *23* (6), 1607−1617.
(17) Peña, M. A.; Fierro, J. L. G. Chemical Structures and Performance of Perovskite Oxides. *Chem. Rev.* **2001**, *101*, 1981−2018.
(18) Dawi, E. A.; Padervand, M.; Ghasemi, S.; Hajiahmadi, S.; Kakaei, K.; Shahsavari, Z.; Karima, S.; Baghernejad, M.; Signoretto, M.; Ibupoto, Z. H.; Tahira, A.; Wang, C. Multi-Functional Fluorinated NiTiO3 Perovskites for CO2 Photocatalytic Reduction, Electrocatalytic Water Splitting, and Biomedical Waste Management. *Journal of Water Process Engineering* **2023**, *54*, 103979.
(19) Zhou, X.; Yan, N.; Chuang, K. T.; Luo, J. Progress in La-Doped SrTiO3 (LST)-Based Anode Materials for Solid Oxide Fuel Cells. *RSC. Advances.* **2014**, *4*, 118−131.
(20) Li, R.; Zhang, C.; Liu, J.; Zhou, J.; Xu, L. A Review on the Electrical Properties of Doped SrTiO3 as Anode Materials for Solid Oxide Fuel Cells. *Materials Research Express* **2019**, *6*, 102006.
(21) Singh, K.; Nowotny, J.; Thangadurai, V. Amphoteric Oxide Semiconductors for Energy Conversion Devices: A Tutorial Review. *Chem. Soc. Rev.* **2013**, *42* (5), 1961−1972.
(22) Miller, D. N.; Irvine, J. T. S. B-Site Doping of Lanthanum Strontium Titanate for Solid Oxide Fuel Cell Anodes. *In Journal of Power Sources* **2011**, *196*, 7323−7327.
(23) Presto, S.; Barbucci, A.; Carpanese, M. P.; Han, F.; Costa, R.; Viviani, M. Application of La-Doped SrTiO3 in Advanced Metal-Supported Solid Oxide Fuel Cells. *Crystals (Basel)* **2018**, *8* (3), 134.
(24) Dong, W.; Yaqub, A.; Janjua, N. K.; Raza, R.; Afzal, M.; Zhu, B. All in One Multifunctional Perovskite Material for Next Generation SOFC. *Electrochim. Acta* **2016**, *193*, 225−230.
(25) Ruosi, A.; Raisch, C.; Verna, A.; Werner, R.; Davidson, B. A.; Fujii, J.; Kleiner, R.; Koelle, D. Electron Sampling Depth and Saturation Effects in Perovskite Films Investigated by Soft X-Ray Absorption Spectroscopy. *Phys. Rev. B Condens Matter Mater. Phys.* **2014**, *90* (12), 1−8.
(26) Fracchia, M.; Ghigna, P.; Pozzi, T.; Anselmi Tamburini, U.; Colombo, V.; Braglia, L.; Torelli, P. Stabilization by Configurational Entropy of the Cu(II) Active Site during CO Oxidation on Mg0.2Co0.2Ni0.2Cu0.2Zn0.2O. *J. Phys. Chem. Lett.* **2020**, *11* (9), 3589−3593.
(27) Shimizu, H.; Toyoshima, R.; Isegawa, K.; Mase, K.; Nakamura, J.; Kondoh, H. A Newly Designed Compact CEY-XAFS Cell in the Soft X-Ray Region and Its Application to Surface XAFS Measurements under Ambient-Pressure Conditions without Photoinduced Side Effects. *Phys. Chem. Chem. Phys.* **2022**, *24* (5), 2988−2996.
(28) Wang, Z.; Toyoshima, R.; Yoshida, M.; Mase, K.; Kondoh, H. In Situ Observation of Charge Transfer in the Cocatalyst-Loaded SrTiO3:Al Photocatalyst under UV Irradiation by Conversion-Electron-Yield Soft-X-Ray Absorption Spectroscopy. *J. Phys. Chem. C* **2024**, *128*, 9193−9201.
(29) Aljaberi, A. D.; Irvine, J. T. S. Ca-Substituted, A-Site Deficient Perovskite La0.2Sr 0.7TiO3 as a Potential Anode Material for SOFCs. *J. Mater. Chem. A Mater.* **2013**, *1* (19), 5868−5874.
(30) Baek, J. Y.; Duy, L. T.; Lee, S. Y.; Seo, H. Aluminum Doping for Optimization of Ultrathin and High-k Dielectric Layer Based on SrTiO3. *J. Mater. Sci. Technol.* **2020**, *42*, 28−37.
(31) Sha, Z.; Kerherve, G.; van Spronsen, M. A.; Wilson, G. E.; Kilner, J. A.; Held, G.; Skinner, S. J. Studying Surface Chemistry of Mixed Conducting Perovskite Oxide Electrodes with Synchrotron-Based Soft X-Rays. *J. Phys. Chem. C* **2023**, *127* (41), 20325−20336.
(32) Li, G.; Li, J.; Li, G.; Jiang, G. N and Ti3+ Co-Doped 3D Anatase TiO2 Superstructures Composed of Ultrathin Nanosheets with Enhanced Visible Light Photocatalytic Activity. *J. Mater. Chem. A Mater.* **2015**, *3* (44), 22073−22080.
(33) Liu, J.; Ma, X.; Yang, L.; Liu, X.; Han, A.; Lv, H.; Zhang, C.; Xu, S. In Situ Green Oxidation Synthesis of Ti3+ and N Self-Doped SrTiOxNy Nanoparticles with Enhanced Photocatalytic Activity under Visible Light. *RSC Adv.* **2018**, *8* (13), 7142−7151.
(34) Bharti, B.; Kumar, S.; Lee, H. N.; Kumar, R. Formation of Oxygen Vacancies and Ti3+ State in TiO2 Thin Film and Enhanced Optical Properties by Air Plasma Treatment. *Nature Scientific Reports* **2016**, *6*, 1−12.
(35) Baek, J. Y.; Duy, L. T.; Lee, S. Y.; Seo, H. Aluminum Doping for Optimization of Ultrathin and High-k Dielectric Layer Based on SrTiO3. *J. Mater. Sci. Technol.* **2020**, *42*, 28−37.
(36) Cavazzani, J.; Squizzato, E.; Brusamarello, E.; Glisenti, A. Exsolution in Ni-Doped Lanthanum Strontium Titanate: A Perovskite-Based Material for Anode Application in Ammonia-Fed Solid Oxide Fuel Cell. *Int. J. Hydrogen Energy* **2022**, *47* (29), 13921−13932.
(37) Adeyemi, A. N.; Venkatesh, A.; Xiao, C.; Zhao, Z.; Li, Y.; Cox, T.; Jing, D.; Rossini, A. J.; Osterloh, F. E.; Zaikina, J. V. Synthesis of SrTiO3 and Al-Doped SrTiO3via the Deep Eutectic Solvent Route. *Mater. Adv.* **2022**, *3* (11), 4736−4747.
(38) Ji, D.; Liu, C.; Yao, Y.; Luo, L.; Wang, W.; Chen, Z. Cerium Substitution in LaCoO3 Perovskite Oxide as Bifunctional Electrocatalysts for Hydrogen and Oxygen Evolution Reactions. *Nanoscale* **2021**, *13* (22), 9952−9959.
(39) Poffe, E.; Kaper, H.; Ehrhardt, B.; Gigli, L.; Aubert, D.; Nodari, L.; Gross, S.; Mascotto, S. Understanding Oxygen Release from Nanoporous Perovskite Oxides and Its Effect on the Catalytic Oxidation of CH4and CO. *ACS Appl. Mater. Interfaces* **2021**, *13*, 25483−25492.
(40) Koo, B.; Kim, K.; Kim, J. K.; Kwon, H.; Han, J. W.; Jung, W. C., Sr Segregation in Perovskite Oxides: Why It Happens and How It Exists. *Joule* **2018**, *2*, 1476−1499.
(41) De Groot, F.; Figueiredo, M.; Basto, M.; Abbate, M.; Petersen, H.; Fuggle, J. 2p X Ray Absorption of Titanium in Minerals. *Phys. Chem. Minerals* **1992**, *19*, 140−147.
(42) De Groot, F. M. F.; Fuggle, J. C.; Thole, B. T.; Sawatzky, G. A. L2,3 x-Ray-Absorption Edges of D0 Compounds: K+, Ca2+, Sc3+, and Ti4+ in Oh (Octahedral) Symmetry. *Phys. Rev. B* **1990**, *41*, 928−937.
(43) Kim, J.; Kim, J. Y.; Park, B. G.; Oh, S. J. Photoemission and X-Ray Absorption Study of the Electronic Structure of SrRu1-x Tix O3. *Phys. Rev. B Condens Matter Mater. Phys.* **2006**, *73* (23), 1−8.
(44) Bunău, O.; Joly, Y. Self-Consistent Aspects of x-Ray Absorption Calculations. *J. Phys.: Condens. Matter* **2009**, *21*, 345501.
(45) Joly, Y. X-Ray Absorption near-Edge Structure Calculations beyond the Muffin-Tin Approximation. *Phys. Rev. B Condens Matter Mater. Phys.* **2001**, *63*, 1−10.
(46) Natile, M. M.; Poletto, F.; Galenda, A.; Glisenti, A.; Montini, T.; De Rogatis, L.; Fornasiero, P. La0.6Sr0.4Co1-YFeyO 3-δ Perovskites: Influence of the Co/Fe Atomic Ratio on Properties and Catalytic Activity toward Alcohol Steam-Reforming. *Chem. Mater.* **2008**, *20* (6), 2314−2327.
(47) Vinai, G.; Motti, F.; Petrov, A. Y.; Polewczyk, V.; Bonanni, V.; Edla, R.; Gobaut, B.; Fujii, J.; Suran, F.; Benedetti, D.; Salvador, F.; Fondacaro, A.; Rossi, G.; Panaccione, G.; Davidson, B. A.; Torelli, P. An Integrated Ultra-High Vacuum Apparatus for Growth and in Situ Characterization of Complex Materials. *Rev. Sci. Instrum.* **2020**, *91* (8), 1−10.

https://doi.org/10.1021/acs.jpclett.4c01900
J. Phys. Chem. Lett. 2024, 15, 8540−8548

(48) Vikatakavi, A.; Mauri, S.; Rivera-Salazar, M. L.; Dobovičnik, E.; Pelatti, S.; D'Addato, S.; Torelli, P.; Luches, P.; Benedetti, S. Role of Metal Dopants in Hydrogen Dissociation on Cu:CeO2 and Fe:CeO2 Surfaces Studied by Ambient-Pressure X-Ray Absorption Spectroscopy. *ACS Appl. Energy Mater.* **2024**, *7*, 2746−2754.
(49) Grinter, D. C.; Ferrer, P.; Venturini, F.; van Spronsen, M. A.; Large, A. I.; Kumar, S.; Jaugstetter, M.; Iordachescu, A.; Watts, A.; Schroeder, S. L. M.; Kroner, A.; Grillo, F.; Francis, S. M.; Webb, P. B.; Hand, M.; Walters, A.; Hillman, M.; Held, G. VerSoX B07-B: A High-Throughput XPS and Ambient Pressure NEXAFS Beamline at Diamond Light Source. *J. Synchrotron Radiat* **2024**, *31*, 578−589.
(50) Castán-Guerrero, C.; Krizmancic, D.; Bonanni, V.; Edla, R.; Deluisa, A.; Salvador, F.; Rossi, G.; Panaccione, G.; Torelli, P. A Reaction Cell for Ambient Pressure Soft X-Ray Absorption Spectroscopy. *Rev. Sci. Instrum.* **2018**, *89* (5), 1−8.

https://doi.org/10.1021/acs.jpclett.4c01900
J. Phys. Chem. Lett. 2024, 15, 8540−8548